Nuclear Science and Techniques (2024) 35:40
https://doi.org/10.1007/s41365-024-01403-7

A compact X-band backward traveling-wave accelerating structure

Xian-Cai Lin[1,2] · Hao Zha[1,2] · Jia-Ru Shi[1,2] · Qiang Gao[1,2] · Fang-Jun Hu[1,2] · Qing-Zhu Li[1,2] · Huai-Bi Chen[1,2]

Received: 20 April 2023 / Revised: 21 August 2023 / Accepted: 31 August 2023 / Published online: 9 April 2024

Abstract
Very high-energy electrons (VHEEs) are potential candidates for FLASH radiotherapy for deep-seated tumors. We proposed a compact VHEE facility based on an X-band high-gradient high-power technique. In this study, we investigated and realized the first X-band backward traveling-wave (BTW) accelerating structure as the buncher for a VHEE facility. A method for calculating the parameters of single cell from the field distribution was introduced to simplify the design of the BTW structure. Time-domain circuit equations were applied to calculate the transient beam parameters of the buncher in the unsteady state. A prototype of the BTW structure with a thermionic cathode-diode electron gun was designed, fabricated, and tested at high power at the Tsinghua X-band high-power test stand. The structure successfully operated with 5-MW microwave pulses from the pulse compressor and outputted electron bunches with an energy of 8 MeV and a pulsed current of 108 mA.

Keywords Backward traveling-wave accelerating structure · Equivalent circuit model · High-power test · Very high-energy electron radiotherapy

1 Introduction

Radiotherapy is an effective way to relieve the cancer burden worldwide [1, 2]. In 2014, scientists reported the superiority of using an ultrahigh dose rate (FLASH) for radiating lung tumors in mice [3]. Subsequently, FLASH-RT has become a topic of particular interest in radiotherapy research [4]. Radiotherapy facilities employing different particles, including photons [5, 6], electrons [7, 8], and protons [9, 10], are underway to apply FLASH radiotherapy in clinical settings. Very high-energy electrons (VHEEs) are considered potential candidates for realizing FLASH radiotherapy for deep-seated tumors in the near future. VHEE radiotherapy, which was first proposed in 2000 [11], utilizes electrons with energies ranging from 50 to 200 MeV [12] to treat tumors to realize fine conformality and reduce treatment time [13, 14]. In recent years, various VHEE radiation experiments have been performed in linear accelerator platforms [15, 16]. Facilities for the future clinical application of VHEE-FLASH radiotherapy were also proposed by the SLAC National Accelerator Laboratory [8] and the Compact Linear Collider (CLIC) radio frequency (RF) group at the European Organization for Nuclear Research (CERN) in collaboration with the Lausanne University Hospital (CHUV) [17]. A research team at Tsinghua University also proposed a compact VHEE facility based on the developed X-band high-gradient technology.

The layout of the proposed compact VHEE facility is illustrated in Fig. 1. The facility is powered by an X-band 50-MW klystron. A pulse compression device enhances the power from the klystron to 150-MW, 300-ns pulses. The linear accelerator includes a buncher and two X-band high-gradient structures. Electrons from a pulsed direct-current (DC) gun were bunched and accelerated to 100 MeV. This VHEE beamline is supposed to deliver 40-Hz, 24 nC/pulse electrons to generate a dose rate of 40 Gy/s at a field of 6 cm × 6 cm, which can be applied in FLASH radiotherapy research. The pulse compression devices and high-gradient structures have been preliminarily studied [18, 19]. This paper introduces research on a prototype of the buncher.

Linear accelerating structures can be divided into three types: standing-wave (SW), traveling-wave (TW), and backward traveling-wave (BTW) structure. The BTW structure is

This work was supported by the National Natural Science Foundation of China (No. 11922504).

✉ Jia-Ru Shi
shij@mail.tsinghua.edu.cn

1 Department of Engineering Physics, Tsinghua University, Beijing 100084, China

2 Key Laboratory of Particle and Radiation Imaging (Tsinghua University), Ministry of Education, Beijing 100084, China

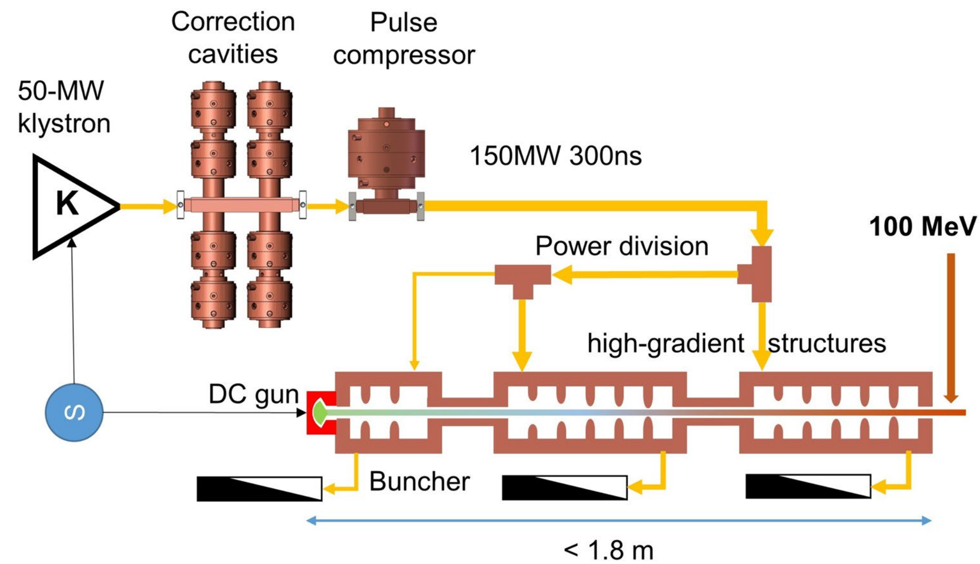

Fig. 1 (Color online) Layout of the compact very high-energy electron facility for radiotherapy

selected as the buncher in this study for the following reasons: compared with the SW structure, the BTW structure can be operated without a circulator, and its filling time is shorter, which is more favorable in the case with a pulse compressor; compared with the TW structure, the BTW can accomplish transverse bunching without a solenoid. Moreover, the BTW structure exhibits a higher shunt impedance than the TW structure. However, BTW structures are less commonly used than SW and TW structures, and only S-band BTW structures have been reported [20–23]. In this study, we expanded the application of BTW structures to a higher frequency (11.424 GHz, X-band).

The remainder of this paper is organized as follows: Sect. 2 introduces the beam dynamics and RF design of the BTW structure. The fabrication and low-power tests of this structure are presented in Sect. 3. In Sect. 4, detailed high-power experimental results are presented. Finally, the conclusions are presented in Sect. 5. The appendices show the existing and developed methods used in this study. Appendix A introduces the equivalent circuit model and illustrates its applications. In Appendix B, we develop a method for calculating the single-cell parameters from the field distribution using the circuit model. This method can be used to design the X-band BTW structure. In Appendix C, we apply the equivalent circuit model in the time domain, which can be used to calculate the transient beam parameters of a buncher. Appendix D presents the beam dynamics equations used in this study.

2 Design of the BTW structure

The X-band BTW structure groups the DC electron beam into bunches (via the bunching section) and accelerates them to approximately 8 MeV (via the accelerating section). The length of the buncher structure in a compact VHEE accelerator should be as short as possible. Since the buncher shares the same power supply system with the X-band high-gradient structure, the filling time of the BTW structure should not be longer than that of the X-band high-gradient structure, which is 95 ns [24].

The beam dynamics design of the BTW structure is similar to that of the SW structure and involves the following steps: First, the cavity shape was optimized. After optimization, the electric field distribution along the *Z*-axis of a single cell with different lengths was calculated to construct the field distribution of the entire structure. The constructed field was used to calculate the beam parameters along the structure. The beam parameters at the exit were optimized by adjusting the length and field amplitude of each cell in the bunching section. Finally, the RF design and simulation were performed to realize the optimized constructed field distribution.

The RF design of a BTW-type buncher is different from that of SW and TW bunchers. The developed method for designing a BTW structure is to simulate the RF parameters of each single cell and then calculate the field distribution of the entire structure using the equivalent circuit model [25]. However, this method ignores the influence of the coupling holes when simulating the single cell. In this study, we introduce a method for calculating the parameters of single cell from the field distribution, simplifying the design process of the BTW structure. This method is described in Appendix B.

The cell shape of the BTW structure is illustrated in Fig. 2. A "nose" structure was adopted to improve the shunt impedance. Coupling holes are shaped like "kidneys" to enable convenient fabrication. Because the input power of this structure is much smaller than that of the high-gradient structure, the shunt impedance and quality factor are not as important. Instead, we focused more on the fabrication and tuning, considering that this is the first fabrication attempt of an X-band BTW structure. The working mode of the structure is selected as 5π/6 to make the first several bunching cells longer, which is beneficial for fabrication and tuning. The accelerating gradient of the accelerating section is set to 44 MV/m, with a maximum surface electric field of approximately 200 MV/m, which proved feasible in the high-gradient experiment [18].

An industrial thermionic cathode-diode electron gun was used as the electron source. The parameters of the DC electron gun are listed in Table 1. An ellipse can be used to represent the electrons emitted from the thermionic cathode in phase space. The geometric emittance is the ellipse area divided by π, and normalized emittance is the geometric emittance multiplied by the normalized momentum of the emission electron. The relevant values in optimizing the beam parameters are the capture rate, energy spread, and phase spread. The capture rate determines the pulsed beam current. As an accelerator used in radiotherapy, the energy spread of a buncher should be as small as possible. Moreover, the phase spread produces an energy spread when the high-gradient structures further accelerate the bunches.

This study uses dynamic equations to calculate the beam parameters, as introduced in Appendix D. The beam dynamics optimization results of the BTW structure are shown in Fig. 3. The average energy of the bunch at the exit is 7.8 MeV, with a capture rate of 32%, as shown in Fig. 3a, b. The root-mean-square (RMS) energy spread is 1.7 MeV, while the RMS phase spread is 13°. During calculation, the electron beam from the DC gun within an RF period is divided into 100 longitudinal slices. Figure 3c shows the phase spaces of each capture slice. The iris radius is 2 mm, and the envelope of the captured electron is within this restriction, as shown in Fig. 3d. The relative phase velocity of a single cell (β_p) is defined as its length divided by the cell's length in the light-speed section, which is 10.93 mm in this BTW structure. After optimization, the β_p values of each cell are shown in Fig. 3e. The β_p of the last cell is set to be larger than 1 to match its length with the width of the standard waveguide. The constructed unloaded and loaded electric field distributions are shown in Fig. 3f.

Table 1 Parameters of the thermionic cathode electron gun

Parameters	Value
Perveance (μP)	0.347
Voltage (kV)	12.5
Emission current (mA)	485
Waist radius (mm)	0.46
Geometric emittance (mm·mrad)	32.7
Normalized emittance (mm·mrad)	7.26

A 3D electromagnetic simulation was performed using the CST Studio suite [26]. Figure 4a shows the vacuum model of the BTW structure. The structure consists of eight cells representing the bunching section and 16 cells representing the accelerating section, to give a total length of 238 mm. The width of the input waveguide was 10.16 mm to match the BJ-100 standard waveguide; therefore, the last cell was lengthened by 0.73 mm. The width of the output waveguide was 3.31 mm, and a step waveguide was designed to match it with a standard waveguide. The input and output couplers both adopted a quasi-symmetric shape to suppress the dipole field.

The model was simulated using a frequency-domain solver at the working frequency point, through which the field distribution along the Z-axis and reflection coefficient at the input port can be obtained. By applying the method introduced in Appendix B, the frequencies of each cell and

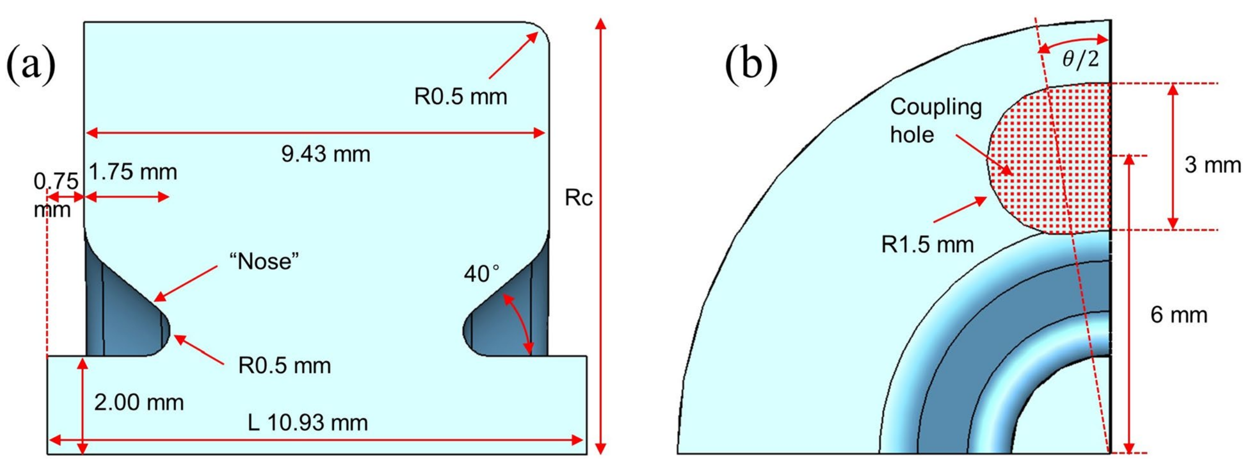

Fig. 2 (Color online) Single-cell model in the accelerating section of the BTW structure: **a** front view of a quarter of the single cell without coupling holes and **b** side view of a quarter of the single cell. The red dotted area shows the shape of the coupling holes between adjacent cells

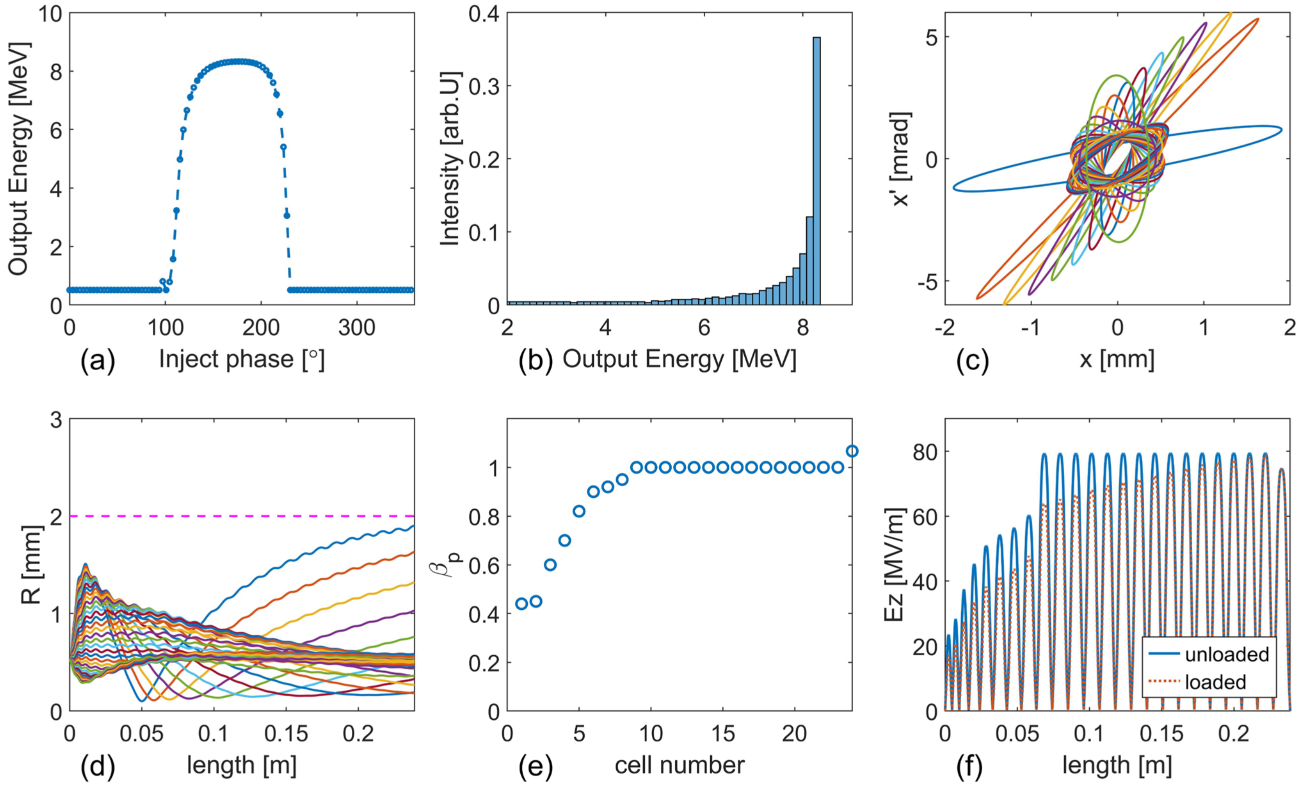

Fig. 3 (Color online) Optimization results of the BTW structure: **a** output electron energy versus injection phase of the DC gun; **b** electron energy distribution at the exit; **c** transverse phase space of different longitudinal slices; **d** transverse envelope of different longitudinal slices along the structure. The dashed line represents the iris radius; (e) the relative phase velocity of each cell; and (f) constructed unloaded and loaded electric field amplitude of the structure after optimization

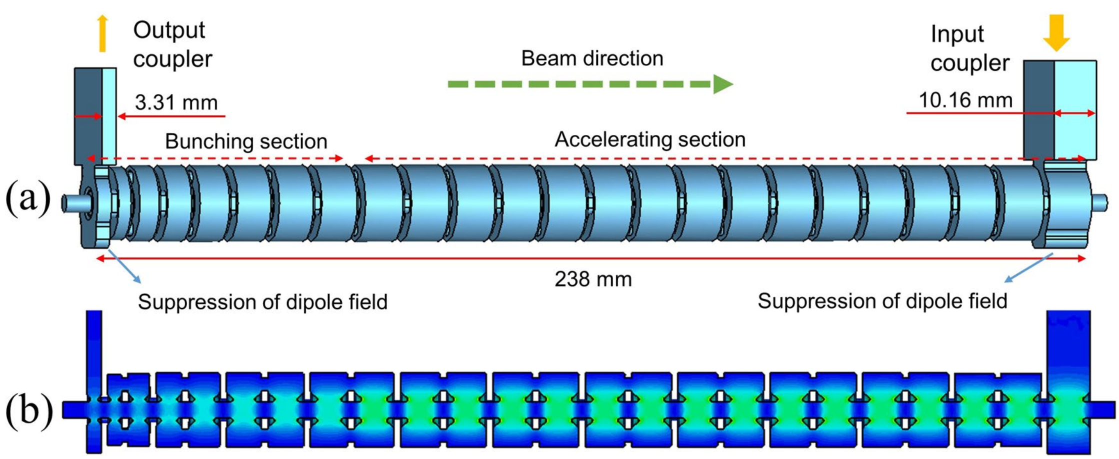

Fig. 4 (Color online) **a** Vacuum model and **b** cross-sectional electric field distribution of the BTW structure

coupling coefficients of adjacent cells can be derived. After repeatedly adjusting the radius and coupling hole of each cell, the simulated cell parameters of the BTW structure converged to the designed values derived from the optimized field distribution, as shown in Fig. 5. The simulated coupling factors of the input and output couplers were 29.3 and 101, respectively. In contrast, their designed values were 29.7 and 102, respectively. The filling time of the structure calculated using Eq. (17) in Appendix B was 95 ns.

When the simulated cell parameters converged to the designed values, the simulated electric field distribution also converged to the designed value. The 2D field

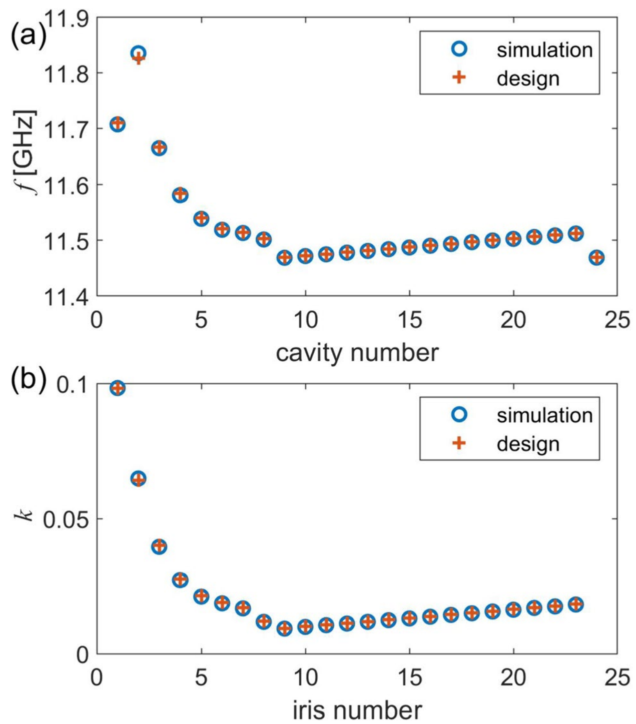

Fig. 5 Single-cell parameters of the BTW structure: **a** the simulated and designed single-cell frequencies and **b** the simulated and designed coupling coefficient between adjacent cells

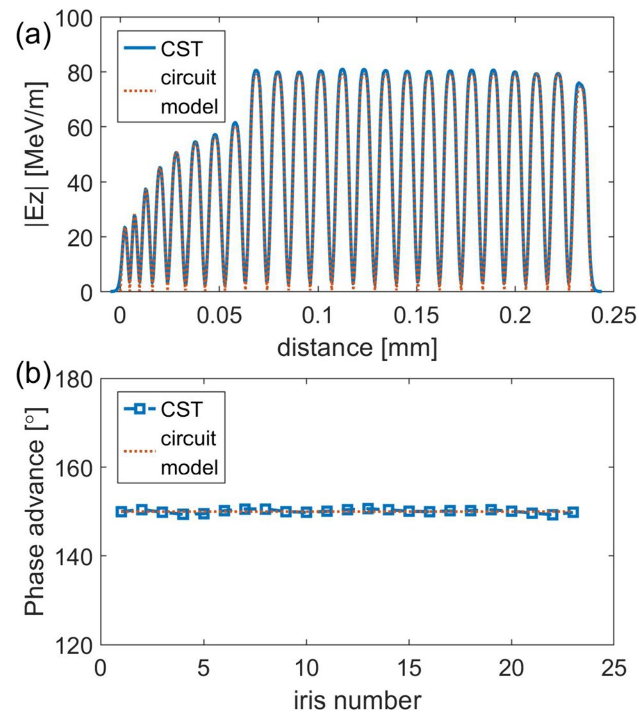

Fig. 6 Electric field of the BTW structure simulated by CST and calculated with equivalent circuit model: **a** electric field amplitude distribution along the *Z*-axis and **b** phase advance of adjacent cells

distribution at the cross-section is shown in Fig. 4b. The longitudinal field distribution on the *Z*-axis is shown in Fig. 6. The field amplitude distribution is nearly the same as the constructed one with the circuit model, and the phase advance is concentrated on the working mode, 5π/6.

The simulated S-parameters in CST are shown in Fig. 7. The simulated reflection coefficient at the working frequency is −40 dB, and the transmission loss is −5.1 dB. The S-parameters calculated using the equivalent circuit model are also presented. The S-parameters fit well in the frequency range next to the working point (11.40–11.47 GHz). Relatively obvious distinctions between the CST and circuit models were observed at higher frequencies, possibly owing to fitting errors in the circuit model and the narrowness of the first several cells.

Figure 8 shows the surface electric field, magnetic field, and modified Poynting vector of the BTW structure. Only the input coupler and two cells are shown because the maximum surface fields are located in the acceleration section. The maximum surface electric field was located at the nose of the cells, whereas the maximum magnetic field and modified Poynting vector were located at the coupling hole between adjacent cells. The maximum field values and other parameters are listed in Table 2.

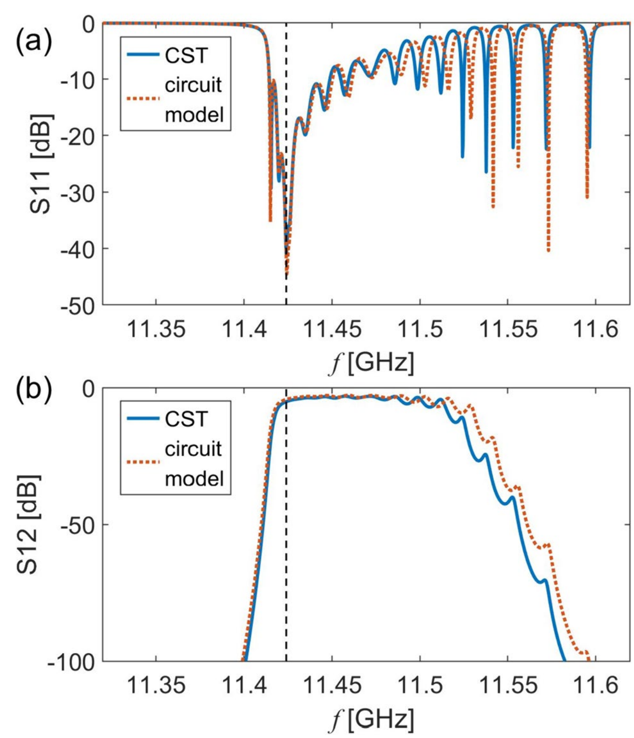

Fig. 7 (Color online) S-parameters of the BTW structure simulated in CST and calculated with the equivalent circuit model: **a** reflection spectrum and **b** transmission spectrum. The black dashed lines denote the working frequency, 11.424 GHz

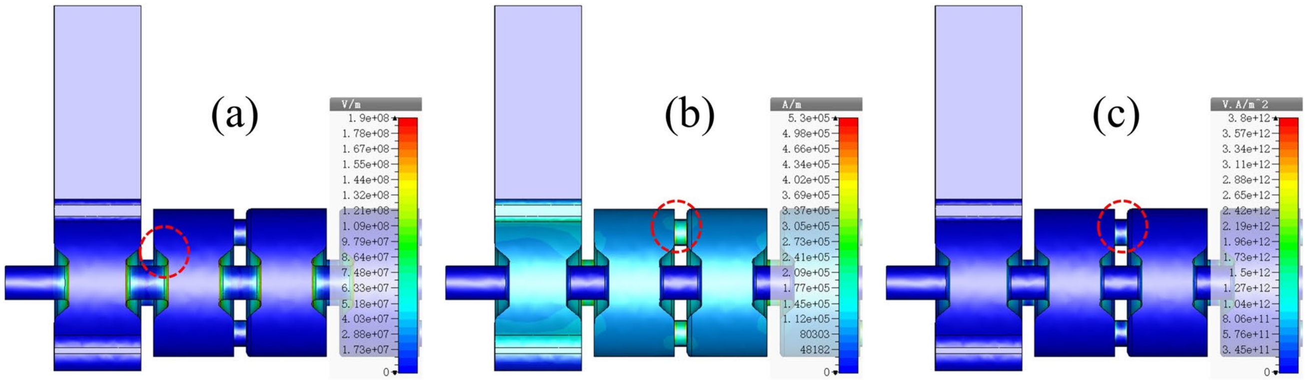

Fig. 8 (Color online) Surface field of the BTW structure at the input section: **a** surface electric field; **b** surface magnetic field; and **c** surface-modified Poynting vector

Table 2 Design and simulated parameters of the BTW structure

Parameters	Value
Cell radius, R_c (mm)	7.72–8.80
Cell length, L (mm)	4.81–10.93
Coupling hole, θ (°)	15.2–33.4
Quality factor Q	3600–6500
Shunt impedance, ZT^2 (MΩ/m)	25.8–139
Group velocity,v_g	0.0051–0.021c
Filling time, t_f (ns)	95
Pulse width, D (ns)	230
Cell's stored energy, u (mJ)	1.1–15.8
Accelerating gradient, E_a (MV/m)	43.6
Peak surface, E (MV/m)	190
Peak surface, H (kA/m)	720
Peak surface, S_c (MW/mm^2)	3.8
Pulse heating, ΔT (K)	105
Reflection, S_{11} (dB)	−40
Transmission, S_{21} (dB)	−5.1

3 Fabrication and low-power test

A 3D computer-aid design (CAD) model of the BTW structure is shown in Fig. 9. The couplers consist of two halves, each processed by the milling machine. The single cell was processed using a lathe, while its coupling holes, cooling channels, and tuning holes were processed using a milling machine. The tuning pins were brazed in the tuning holes for tuning during low-power measurements. After machining, each part was brazed for further testing.

After fabrication, RF measurements were applied to the structures. Bead-pull field measurements were performed to tune the structure, as shown in Fig. 10. The details of the experimental setup are similar to those in Ref. [18]. According to the nonresonant perturbation theory [27], the electric field is proportional to the square root of the reflection variations in the presence and absence of a perturbing object.

After obtaining the field distribution, the tuning method for nonuniform TW accelerating structures [28] was

Fig. 9 (Color online) Engineering design of the BTW structure: **a** CAD model of the whole BTW structure; **b** the output coupler with a step waveguide; **c** the single cell with cooling channels and tuning pins; and **d** the input coupler

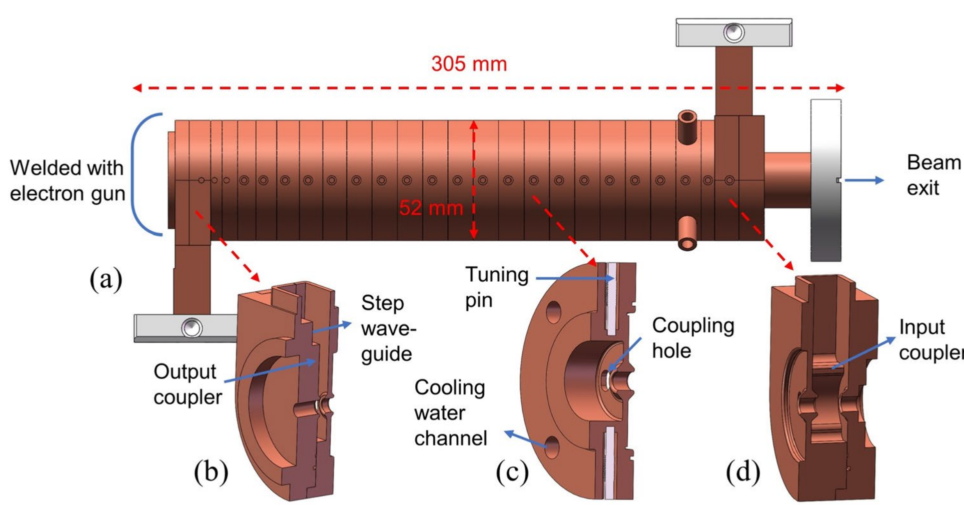

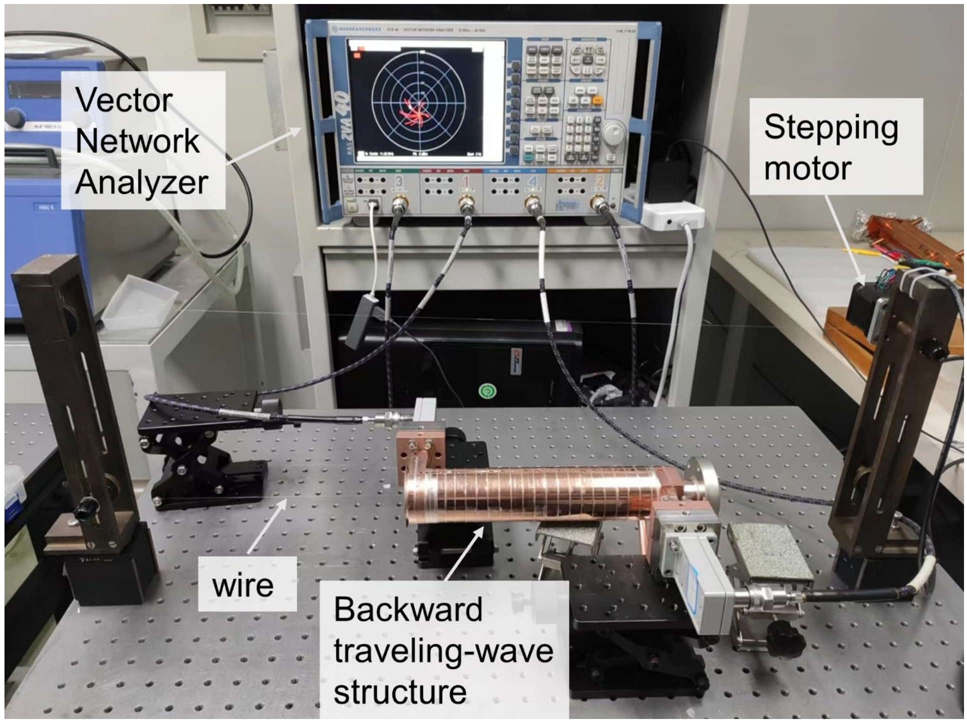

Fig. 10 (Color online) Field measurement of the BTW structure

applied. Based on the tuning method, the frequency of the cells in the accelerating section was approximately 4 MHz below the designed value. Therefore, we tuned the cells by pushing the tuners onto the structure. However, the measurement results showed that the frequency of the first cell (i.e., the output coupler) was approximately 50 MHz lower than the designed value, which was beyond the tuning range. This frequency shift was previously evaluated as a fabrication deviation because of a lack of experience. To reduce the influence of the deviation on this BTW structure, we tuned the cells of the bunching section away from the designed frequencies to counteract part of the reflection from the first cell. This machining fault can be avoided in the future by conducting more detailed checks during the low-power tests.

The field measurement results before and after tuning are shown in Fig. 11. Before tuning, the average phase advance of the accelerating section was 144°. After tuning, this value is about 150°, corresponding to the working mode, 5π/6. Because of the fabrication error of the first cell, the field distribution of the bunching section was different from that of the designed section. We used the measured results after tuning to calculate the beam dynamics, with the capture rate decreasing from 32 to 25%. This is acceptable for a prototype; however, more careful machining and checking should be performed in the future. The S-parameters after tuning are shown in Fig. 12; the reflection on the working frequency is − 25 dB, and the transmission loss is − 5.1 dB.

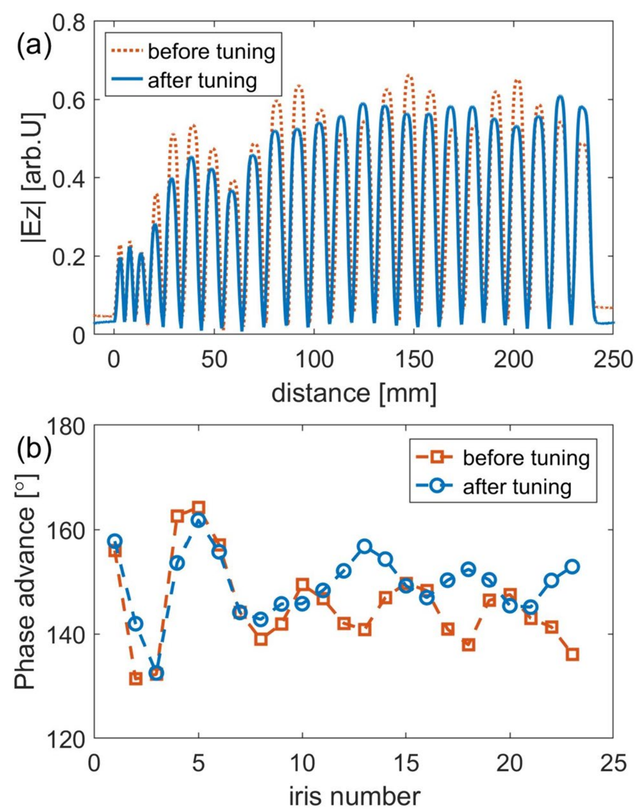

Fig. 11 (Color online) Field measurement results before and after tuning: **a** relative field amplitude distribution and **b** phase advances measurement results

4 High-power test

After the low-power microwave test, the thermionic cathode electron gun was welded to the BTW structure. The structure was then installed and subjected to high-power testing at the Tsinghua X-band high-power test stand (TpoT-X) [29]. The high-power experimental setup is shown in Fig. 13. A previous study tested an X-band two-stage pulse compression system with a correction cavity chain at TpoT-X [19]. The BTW structure was installed at the output of the pulse compression system. The pulse compression system can output a three-time, 230-ns flattop pulse in the one-stage pulse compression mode (with the second compressor detuned). The one-stage output is used as the input pulse for the BTW structure.

An RF waveguide window was installed between the pulse compressor and BTW structure to avoid interference in the vacuum inside the two systems, as shown in Fig. 13a. A high voltage was applied to the thermionic cathode using an electron gun power supply. A titanium window was installed at the exit of the structure. The beam was tested and measured under atmospheric conditions.

The structure was conditioned after installation, and the system operated at a repetition rate of 40 Hz. When the vacuum was worse than 1×10^{-5} Pa or the reflection from the structure was five times larger than the normal one, the auto-conditioning system recorded it as a breakdown event and shut down the microwave source for 30 s. If the structure operated without breakdown for 60 s, the klystron output increased by a set value. After conditioning with 2.2×10^{6} pulses, the BTW structure reached a maximum input power of 5.5 MW. After conditioning, the BTW structure operated with an input power of 5 MW for 4.2×10^{5} pulses, and a breakdown rate of 2×10^{-4}/pulse was recorded. Therefore, the high-power performance of the BTW structure was verified. Subsequently, the thermionic cathode was activated. The measured pervelance of the electron gun was 0.315 μP, which is 10% smaller than the designed value. Beam tests were conducted after activation.

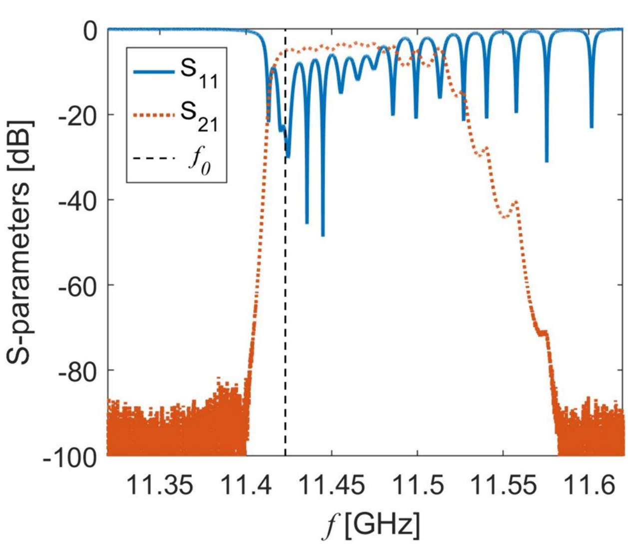

Fig. 12 (Color online) S-parameters of the BTW structure after tuning. The blue solid line is the reflection spectrum. The red dotted line is the transmission spectrum. The black dash line denotes the working frequency

The measurement results are shown in Fig. 14. The waveforms obtained during the high-power tests are presented in Fig. 14a. Among them, the input, output, and reflected waves were measured using a directional coupler, and the beam current was collected by a current collector. The input wave was a 5-MW pulse from a pulse compressor. The output pulse was about 100 ns later than the input pulse. Owing to the dispersion effect, the shape of the output pulse differs from that of the input pulse. The pulsed beam current has similarities with the output wave in terms of transient behavior. Both pulses are magnified and plotted in Fig. 14b. The pulsed beam current can be roughly divided into a rising edge (1000–1130 ns), a steady state (1130–1190 ns), and a falling edge (1190–1260 ns), which is in accordance with the output pulse. According to the equivalent circuit model, the output pulse reflects the field in the first cell. Therefore, when the first cell reaches the steady state, the beam current also does. The falling edge of the beam current is earlier than the output pulse because the cells behind the first cell, whose field also influences the bunching process, reach the falling edge earlier than the first cell. The steady state of the beam current is short because of the long filling time and short input pulse. The current waveform calculated from the measured input wave using the time-domain circuit equation introduced in Appendix C is shown in Fig. 14b. The calculated pulsed current wave fundamentally fits the measured value; however, any discrepancy between the calculated and measured pulse currents may be due to the inaccuracy of the transient beam loading calculation method.

A bending magnet is typically used to measure the energy of a charged-particle bunch. However, the magnet was too large for installation at the exit of the BTW structure on our platform. Therefore, a series of steel sheets were used to measure the range of the electron beam and calculate its energy. The experimental setup is shown in Fig. 13b. The measurement results are shown in Fig. 14c. The practical range is 3.95 g/cm^2. According to the standard GB/T 25306–2010, the most probable energy source is:

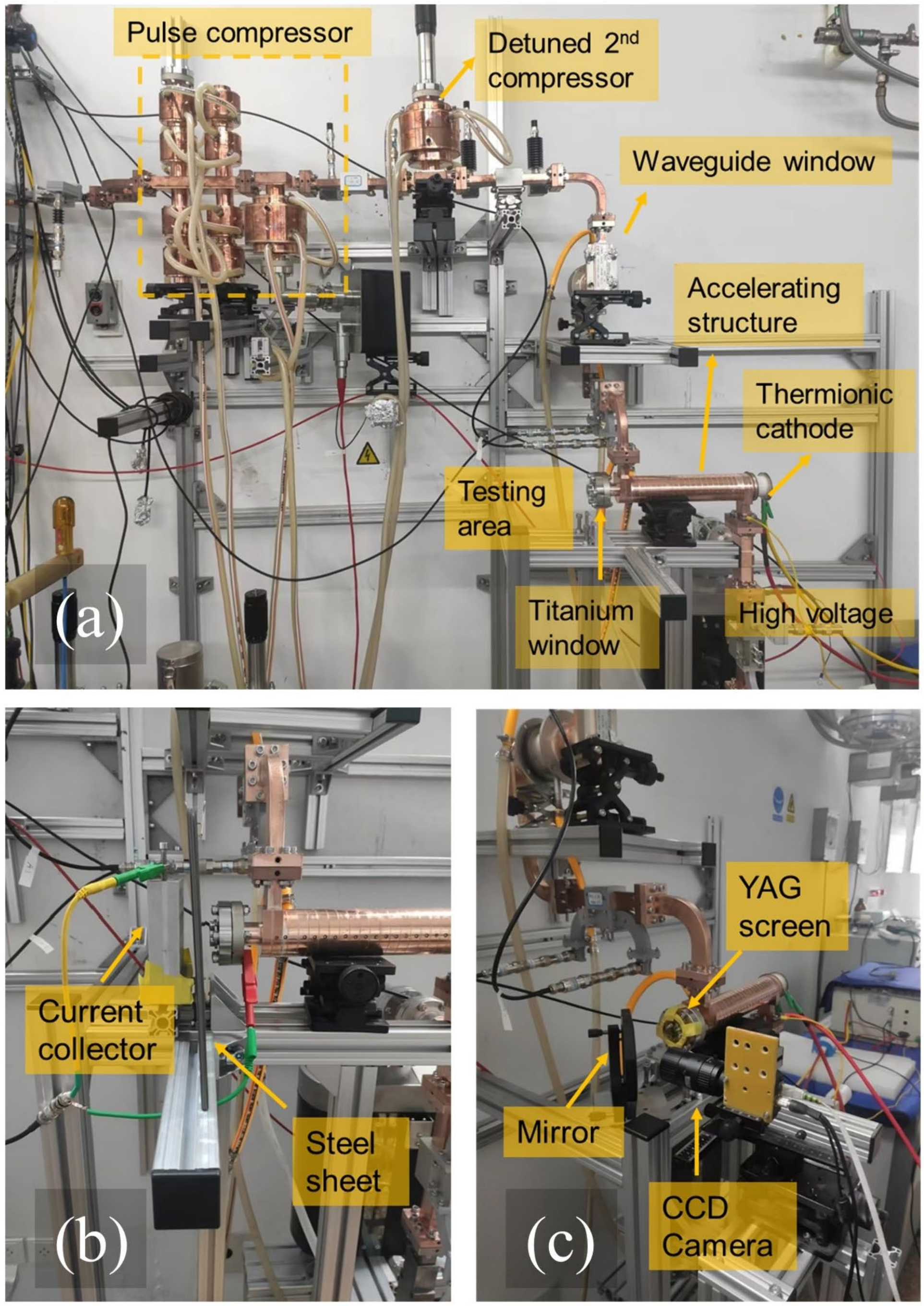

Fig. 13 (Color online) High-power beam test of the BTW structure: **a** high-power experiment setup, **b** pulsed beam current and beam energy measurement, and **c** transverse beam distribution measurement

$$E_p = 0.22 + 1.98R_p + 0.0025R_p^2, \quad (1)$$

where E_p is in MeV, and R_p is in g/cm^2. Consequently, the measured beam energy is 8.01 MeV.

The beam spot was measured using a yttrium aluminum garnet (YAG) screen and recorded using a charge-coupled device (CCD) camera, as shown in Fig. 13c. The beam projection image after the pseudo-color processing, the beam density distributions at the X and Y cross-sections at the beam center (indicated by the green lines), and the Gaussian fitting curves (indicated by the red lines) are shown in Fig. 14d. According to the fitting results, the RMS radii of the beam are 1.0 and 0.95 mm in the X- and Y-direction, respectively.

A comparison of the designed and measured values of the BTW structure is presented in Table 3. Considering the loss of waveguide and quality factor degradation of the structure after fabrication, its input power was set to 5.0 MW, which was higher than the design value of 4.6 MW. The accelerating gradient was calculated by dividing the beam energy at

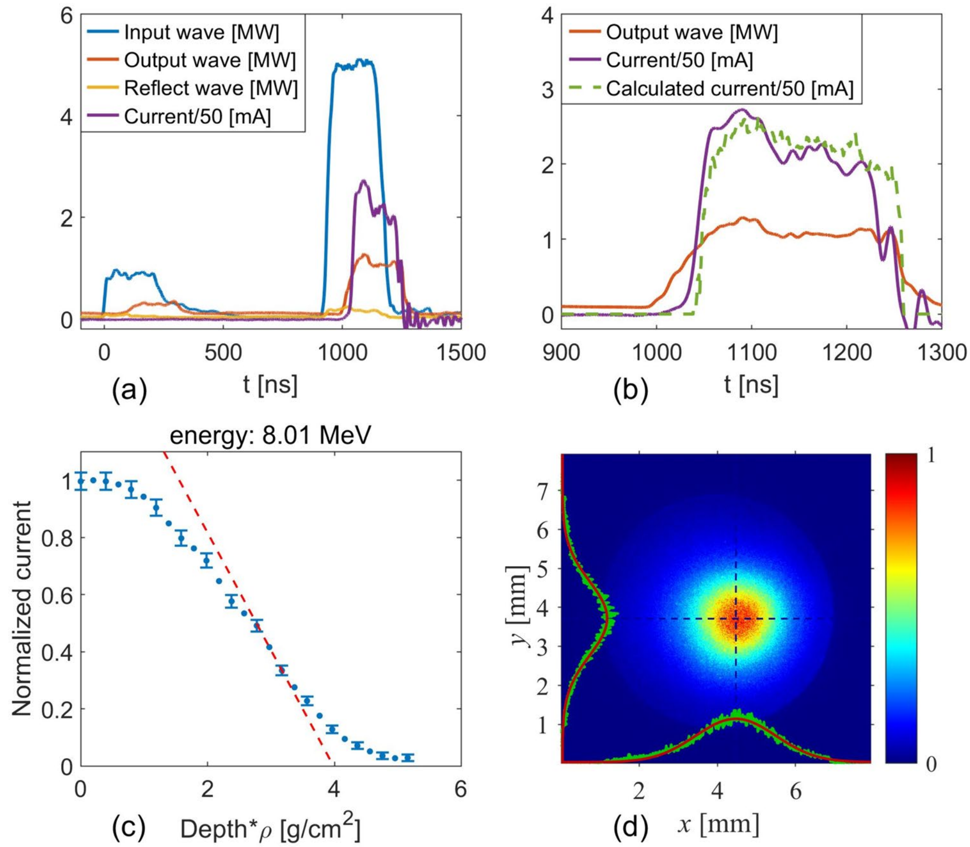

Fig. 14 (Color online) High-power test results of the BTW structure: **a** input, output, reflect, and pulsed current waveform during the high-power experiment; **b** magnified output waveform, pulsed current waveform, and calculated current with measured input pulse; **c** energy measurement with a stack of steel sheets; and **d** transverse distribution of the beam at the exit. Green lines are distributions at the cross-section, and red lines are their Gaussian fitting curves

the exit by the length of the structure. The measured value was 3% higher than the designed value. The breakdown rate is 2×10^{-4}. A lower breakdown rate must be attained to apply this buncher in a radiotherapy scenario. In the future, rounding the coupling hole should be considered to reduce the breakdown rate. The measured pulsed current was smaller than the designed value because of the decreased capture ratio and electron gun emission. Although the beam parameters, including the current and beam spot, were not as good as the design, the high-gradient and large-current performances of the BTW structure were preliminarily verified. In the future, we will attempt to correct the fabrication error of the output coupler to ensure that the capture ratio is as designed, and the magnetic coupling holes between adjacent cells will be optimized with smooth rounding [22] to improve its high-gradient performance.

Table 3 Comparison of the designed and measured values of the BTW structure

Parameters	Designed value	Measured result
Input power (MW)	4.6	5.0
Accelerating gradient (MV/m)	43.6	45.0
Breakdown rate (/pulse)	–	2×10^{-4}
Capture ratio	32%	25%
Current (mA)	155	108
Energy (MeV)	7.8	8.0
r_x (RMS) (mm)	0.69	1.0
r_y (RMS) (mm)	0.69	0.95

5 Conclusion

This study presents the prototype X-band BTW accelerating structure for future very high-energy electron radiotherapy facilities. A method for calculating the parameters of single cell using field distribution was derived to simplify the design process. The BTW structure was simulated and designed in the CST using this method after dynamic beam optimization. The simulated field distribution fits well with the constructed distribution. A time-domain circuit equation was applied to analyze the transient beam parameters of the buncher in the unsteady state. The BTW structure was fabricated at Tsinghua University and high-power tested at the Tsinghua X-band high-power test stand. The structure was powered with 5-MW microwave pulses from a pulse compressor, with an average gradient of 45 MV/m. The electron bunches were accelerated to 8 MeV with a pulsed current of 108 mA. Both the high-gradient and large-current performance of the BTW structure were proven preliminarily in the high-power experiment.

Appendix A: Equivalent circuit model of a coupled cavity chain

The equivalent circuit model has been an important tool for analyzing coupled cavity chains [30–34]. It can be applied to calculate the field distribution from single-cell parameters [25] and to analyze cavity detuning during measurements [35]. The equations for the equivalent circuit model of the coupled cavity chain are expressed in Eq. (2).

$$\begin{bmatrix} \lambda_1 & -\frac{k_1}{2} & & & \\ & \ddots & & & \\ & -\frac{k_{i-1}}{2} & \lambda_i & -\frac{k_i}{2} & \\ & & & \ddots & \\ & & & -\frac{k_{n-1}}{2} & \lambda_n \end{bmatrix} \begin{bmatrix} X_1 \\ \vdots \\ X_i \\ \vdots \\ X_n \end{bmatrix} = \begin{bmatrix} I_1 \\ \vdots \\ I_i \\ \vdots \\ I_n \end{bmatrix} \tag{2}$$

In this equation, k_i is the coupling coefficient between cells i and $i+1$. The expressions λ_i, X_i, and I_i are different for the magnetic and electric coupling models. Here, we use subscript m and e to denote them, respectively:

$$\lambda_{m,i} = 1 - j\frac{\omega_i(1+\beta_i)}{\omega Q_i} - \frac{\omega_i^2}{\omega^2},\ \lambda_{e,i} = 1 + j\frac{\omega(1+\beta_i)}{\omega_i Q_i} - \frac{\omega^2}{\omega_i^2}, \tag{3}$$

where ω is the angular frequency of the input microwave, ω_i is the resonant angular frequency of single cell, Q_i is the quality factor, and β_i is the coupling factor with the outer waveguide. As the solution of Eq. (2), X_i is related to the electric field of cell i [21].

$$X_{m,i} = V_i \cdot \frac{j\omega}{\omega_i}\sqrt{\frac{Q_i}{Z_i\omega_i}},\ X_{e,i} = V_i \cdot j\omega\sqrt{\frac{Q_i}{Z_i\omega_i}}. \tag{4}$$

Here, V_i is the maximum accelerating voltage of cell i, and Z_i is the shunt impedance. I_i in Eq. (2) is a source term related to the input power and beam loading.

$$\begin{aligned} I_{m,i} &= \frac{2}{j\omega}\sqrt{\frac{\omega_i P_i \beta_i}{Q_i}} - i_i\frac{\omega_i}{\omega^2}\sqrt{\frac{Z_i T_i^2 \omega_i}{Q_i}}, \\ I_{e,i} &= 2j\omega\sqrt{\frac{P_i\beta_i}{\omega_i Q_i}} + i_i\sqrt{\frac{Z_i T_i^2\omega_i}{Q_i}}, \end{aligned} \tag{5}$$

where T_i is the transit time factor, i_i is the loaded current, and P_i is the input power. According to Eq. (2), if the RF parameters of each cell, that is, ω_i, k_i, β_i, Z_i, Q_i, are obtained

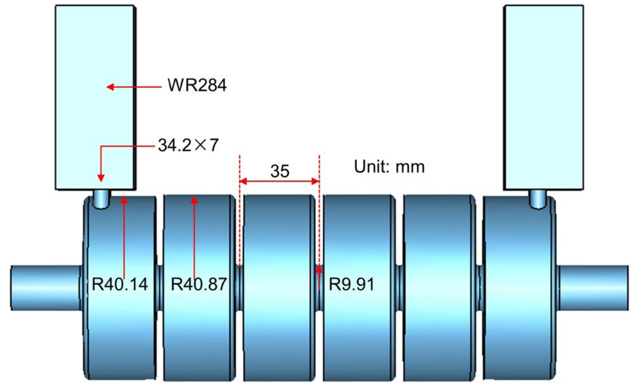

Fig. 15 (Color online) Dimensions of the example TW structure

Table 4 Single-cell parameters of the example TW structure

Parameters	cell 1, 6	cell 2–5
f (MHz)	2853.3	2849.9
k	0.0106	0.0106
Q	1.44×10^4	1.44×10^4
Z (MΩ)	2.68	2.68
β	63	

from the isolated single-cell model, then V_i can be calculated without simulating the entire structure.

An equivalent circuit model can also be applied to calculate the reflection and transmission spectra. Assuming the input and output coupler are located in cells 1 and n, respectively, the reflection and transmission coefficients can be derived by analyzing the voltages in the equivalent circuit model with the outer coupling:

$$\Gamma_m = 1 + 2j\frac{\beta_1\omega_1 X_1}{I_1\omega Q_1},\ \Gamma_e = 1 - 2j\frac{\beta_1\omega X_1}{I_1\omega_1 Q_1} \tag{6}$$

$$T_m = -2j\frac{\sqrt{\omega_1\omega_n}X_n}{I_1\omega\sqrt{Q_{e,1}Q_{e,n}}},\ T_e = 2j\frac{\beta_n\omega X_n}{I_1\sqrt{\omega_1\omega_n}\sqrt{Q_{e,1}Q_{e,n}}} \tag{7}$$

To illustrate the function of the circuit model more visibly, we simulated an S-band (2856 MHz) 6-cell constant impedance TW structure and compared it with the calculation results of the circuit model. The dimensions of the example TW structure are shown in Fig. 15, the single-cell parameters are listed in Table4, and the simulation results are shown in Fig. 16.

The S-parameters fit very well, as shown in Fig. 16b, d, which indicates that the equivalent circuit model can serve as a method to quickly calculate the spectra of the coupled cavity chain. The circuit model can be used to calculate the field distribution as discrete complex values for each cell,

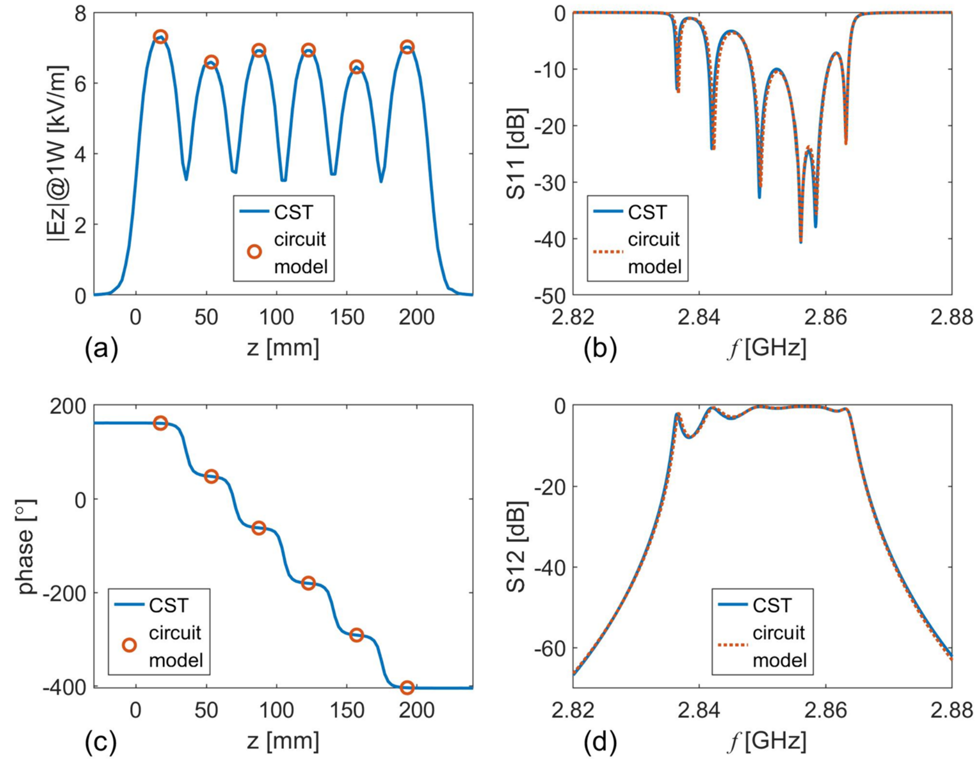

Fig. 16 (Color online) Fields and S-parameters of the example TW structure simulated by CST and calculated using the equivalent circuit model: **a** longitudinal field distribution; **b** reflection spectrum; **c** phase of the longitudinal field; and **d** transmission spectrum

as shown in Fig. 16a, c. For the SW or BTW structures, an intact field distribution can be constructed using the fields of each cell, which can be further used to calculate the beam dynamics. For TW structures, because there are non-negligible fields at the interface between adjacent cells, there will be non-continuity in the constructed field when the field amplitudes of the adjacent cells are different. Therefore, to the best of our knowledge, this circuit model has not been applied to calculate the beam dynamics in TW structures with a bunching section.

Appendix B: Calculating single-cell parameters from field distribution

The single-cell parameters must be determined before utilizing the equivalent circuit model. Among them, Z_i and Q_i were not sensitive to the cell dimensions, whereas ω_i, k_i, and β_i were very sensitive. Furthermore, ω_i, k_i, and β_i are affected by their adjacent cells and are therefore not accurate when obtained from the isolated single-cell model. In this study, we developed a method for obtaining the RF parameters of each cell from the field distribution of the entire structure. This method can determine the RF parameters of each cell from the optimized field distribution in the beam dynamic design or from the simulated distribution in the 3D model to guide the size adjustment of each cell. A simplified version of this method was previously studied [36] without considering loss and couplers. This study removes these simplifications and expands the method to the TW or BTW structure.

In this method, the Z_i and Q_i values of the single cell are calculated beforehand from the isolated model. The field distribution is obtained from beam dynamic calculations or RF simulations, that is, X_i is known. The problem then becomes calculating the $\omega_i, k_i, \beta_1, \beta_n$ using the given X_i. As the equations in Eq. (2) are complex, there are $2n$ equations, including the real and imaginary parts. However, if the number of unknown parameters is $2n+1$. One of the parameters can be set to calculate the rest parameters. Herein, we assume that the k_1 is known. In the following, we first show the solution process and explain how to choose or calculate k_1.

The following analyses are based on the BTW structure. The derivation procedure for the TW structure is very similar and is not shown in this study. For a BTW structure, electrons are injected into the cell of the output coupler; therefore, we denote this cell as Cell 1. As this method does not involve beam loading, only I_n in Eq. (5) is non-zero, which is simplified as:

$$I_n = \frac{2}{j\omega}\sqrt{\frac{\omega_n P_s \beta_n}{Q_n}}. \tag{8}$$

The real and imaginary parts of the first equation in Eq. (2) can be written as:

$$\begin{cases} 1-\dfrac{\omega_1^2}{\omega^2}=\dfrac{k_1}{2}\mathrm{Re}\left(\dfrac{X_2}{X_1}\right) \\ -\dfrac{\omega_1(1+\beta_1)}{\omega Q_1}=\dfrac{k_1}{2}\mathrm{Im}\left(\dfrac{X_2}{X_1}\right) \end{cases} \tag{9}$$

Because k_1 is known, ω_1 and β_1 can be calculated directly as:

$$\begin{cases} \omega_1=\omega\sqrt{1-\mathrm{Re}\left(\dfrac{k_1}{2}\dfrac{X_2}{X_1}\right)} \\ \beta_1=-\dfrac{\omega Q_1}{\omega_1}\mathrm{Im}\left(\dfrac{k_1}{2}\dfrac{X_2}{X_1}\right)-1 \end{cases} \tag{10}$$

Similarly, the equations of middle cells in Eq. (2) can be written as:

$$\begin{cases} 1-\dfrac{\omega_i^2}{\omega^2}=\mathrm{Re}\left(\dfrac{k_{i-1}}{2}\dfrac{X_{i-1}}{X_i}+\dfrac{k_i}{2}\dfrac{X_{i+1}}{X_i}\right) \\ -\dfrac{\omega_i}{\omega Q_i}=\mathrm{Im}\left(\dfrac{k_{i-1}}{2}\dfrac{X_{i-1}}{X_i}+\dfrac{k_i}{2}\dfrac{X_{i+1}}{X_i}\right) \end{cases} \tag{11}$$

For cell i, k_{i-1} is known because the equations are successively solved from 1 to n. Then, k_i and ω_i can be calculated as:

$$\begin{cases} k_i=-\left(\dfrac{2\omega_i}{\omega Q_i}+\mathrm{Im}\left(k_{i-1}\dfrac{X_{i-1}}{X_i}\right)\right)\Bigg/\mathrm{Im}\left(\dfrac{X_{i+1}}{X_i}\right) \\ \omega_i=\omega\sqrt{1-\mathrm{Re}\left(\dfrac{k_{i-1}}{2}\dfrac{X_{i-1}}{X_i}+\dfrac{k_i}{2}\dfrac{X_{i+1}}{X_i}\right)} \end{cases} \tag{12}$$

The calculation of Eq. (12) is iterative. First, we set $\omega_i/\omega=1$ to calculate k_i and then iteratively calculate ω_i and k_i until convergence.

Owing to the source term I_n, solving cell n differs from solving the others. To simplify this equation, use the reflection coefficient in Eq. (6) and substitute 1 with n (the input coupler is denoted as Cell 1 in Eq. (6); however, we denote it as cell n in this section), then we obtain:

$$\frac{I_n}{X_n}=\frac{2j\omega_n\beta_n}{\omega Q_n(\Gamma-1)}. \tag{13}$$

Then, the equation of cell n can be written as:

$$\begin{cases} 1-\dfrac{\omega_n^2}{\omega^2}+\dfrac{2b\omega_n\beta_n}{\omega Q_n}=\dfrac{k_{n-1}}{2}\mathrm{Re}\left(\dfrac{X_{n-1}}{X_n}\right) \\ -\dfrac{\omega_n(1+\beta_n+2a\beta_n)}{\omega Q_n}=\dfrac{k_{n-1}}{2}\mathrm{Im}\left(\dfrac{X_{n-1}}{X_n}\right) \end{cases}, \tag{14}$$

where a and b denote the real and imaginary parts of $1/(\Gamma-1)$, respectively. Therefore, ω_n and β_n can be calculated as:

$$\begin{cases} \omega_n=\omega\sqrt{1+\dfrac{2b\omega_n\beta_n}{\omega Q_n}-\dfrac{k_{n-1}}{2}\mathrm{Re}\left(\dfrac{X_{n-1}}{X_n}\right)} \\ \beta_n=\left(\dfrac{\omega Q_n}{\omega_n}\dfrac{k_{n-1}}{2}\mathrm{Im}\left(\dfrac{X_{n-1}}{X_n}\right)-1\right)\Bigg/(1+2a) \end{cases}. \tag{15}$$

The calculation of Eq. (15) is also iterative. First, we set $\omega_n/\omega=1$ to calculate ω_n and then iteratively calculate β_n and ω_n until convergence. Combining Eqs. (10), (12) and (15), the $\omega_i, k_i, \beta_1, \beta_n$ can be solved using a given field distribution and k_1.

Next, we explain how to choose or calculate the k_1. This is illustrated in two application scenarios.

The first one is to determine the RF parameters of each cell from the optimized field distribution in the beam dynamic calculation. $\Gamma=0$ was set in this case because the structure is supposed to operate without reflection when it reaches the steady state. Therefore, in Eq. (15) $a=-1,\ b=0$. In designing the structure, k is an important factor that affects the filling time and efficiency. The relationship between the coupling coefficient and group velocity is:

$$v_{g,i}=\frac{k_i^*}{2}\omega_i D_i\sin\theta, \tag{16}$$

where $v_{g,i}$ is the group velocity of cell i; D_i is the cell's length; θ is the working mode; and k_i^* is the coupling coefficient of cell i. In a buncher, the coupling holes on the two sides of the cell are different, and k_i^* can be approximated as $(k_{i-1}+k_i)/2$. The filling time of the entire structure can be estimated using [37]:

$$t_f=\sum\frac{D_i}{v_{g,i}}. \tag{17}$$

With a smaller coupling coefficient, the group velocity is smaller and the electric field is higher for a given power supply [37], while the filling time is longer. An appropriate k value can be selected by considering the filling time and efficiency.

The second application scenario involves obtaining the RF parameters of each cell from the simulated field distribution in the 3D model. First, the phase of the simulated Γ

should be determined. According to the equivalent circuit model, Γ is the reflection coefficient on the detuned open plane. Therefore, the simulated Γ value should be divided by the reflection coefficient when the coupler is detuned. When solving the equations, different k_1 values lead to different sets of cell parameters. By substituting these parameters into Eq. (2), we obtained the calculated absolute value of the field distribution. Different k_1 values correspond to different field values, and only one field value is equal to that in the simulation. Thus, we used the power information to calculate the k_1 of the simulated model. Furthermore, by utilizing an additional field distribution, such as the distribution when power is fed from the output coupler or the distribution at another frequency, all parameters can be calculated without the power information, which can be applied to the low-power measurement of the structure.

After obtaining the cell parameters, the cell size can be adjusted by comparing them with the designed parameters. The deviations in ω_i, k_i, and β_i can be compensated for by adjusting the radius, coupling hole, and coupler of cell i, respectively. This method is essentially a reversible transformation that converts the field distribution into cell parameters that are easier to compensate for. When the cell parameters of a simulated structure converge to the designed values, the field distribution also converges to the designed values.

Appendix C: Applying the equivalent circuit model in the time domain

By applying the beam loading term to Eq. (5), the field distribution under beam loading can be calculated by solving the equivalent equations. In a buncher, the loaded current is calculated by setting an initial value and iteratively solving Eq. (2) and calculating the capture ratio using the field distribution. However, as a calculation method in the frequency domain, the equivalent circuit equation can only be used to calculate the steady-state field distribution. For a structure operating with short pulses, the field and beam parameters in the unsteady state were also considered. This section introduces a method for applying an equivalent circuit model to the time domain.

By applying Fourier transformation, Eq. (2) can be transformed into a time-domain equation. Consider the following equation for the first cell as an example:

$$\left(1 - j\frac{\omega_1(1+\beta_1)}{\omega Q_1} - \frac{\omega_1^2}{\omega^2}\right)X_1 - \frac{k_1}{2}X_2 = 0. \tag{18}$$

Multiplying both sides of the equation by ω^2 and applying Fourier transformation. Let $v_i = \mathcal{F}^{-1}\{X_i\}$, then $\mathcal{F}^{-1}\{j\omega X_i\} = \mathrm{d}v_i/\mathrm{d}t$, $\mathcal{F}^{-1}\{-\omega^2 X_i\} = \mathrm{d}^2v_i/\mathrm{d}t^2$. Equation (18) is transformed into

$$\left(-\frac{\mathrm{d}^2v_1}{\mathrm{d}t^2} - \frac{\omega_1(1+\beta_1)}{Q_1}\frac{\mathrm{d}v_1}{\mathrm{d}t} - \omega_1^2 v_1\right) + \frac{k_1}{2}\frac{\mathrm{d}^2v_2}{\mathrm{d}t^2} = 0. \tag{19}$$

In this way, Eq. (2) can be transformed into a second-order differential equation. However, numerically solving these equations is difficult. Next, we simplify the equation by transforming it into an amplitude equation and removing the second-order differential term. First, v_i can be written as

$$v_i = V_i e^{j\omega t}, \tag{20}$$

where V_i is the complex amplitude. Then

$$\frac{\mathrm{d}v_i}{\mathrm{d}t} = \left(\frac{\mathrm{d}V_i}{\mathrm{d}t} + j\omega V_i\right)e^{j\omega t}, \tag{21}$$

$$\frac{\mathrm{d}^2v_i}{\mathrm{d}t^2} = \left(\frac{\mathrm{d}^2V_i}{\mathrm{d}t^2} + j2\omega\frac{\mathrm{d}V_i}{\mathrm{d}t} - \omega^2 V_i\right)e^{j\omega t}. \tag{22}$$

Applying them to Eq. (19), $e^{j\omega t}$ can be removed. Moreover, for V_i, the variation in one period was significantly less than its amplitude. This is also true for the derivation of V_i. Therefore,

$$\frac{1}{\omega}\frac{\mathrm{d}V_i}{\mathrm{d}t} \ll V_i,\quad \frac{1}{\omega}\frac{\mathrm{d}^2V_i}{\mathrm{d}t^2} \ll \frac{\mathrm{d}V_i}{\mathrm{d}t}. \tag{23}$$

Under this assumption, the second-order differential term can be eliminated. Moreover, k_i is usually much less than 1, and the first-order differential term of V_2 can also be removed. Then, Eq. (19) can be simplified as follows:

$$\left(1 - j\frac{\omega_1(1+\beta_1)}{\omega Q_1} - \frac{\omega_1^2}{\omega^2}\right)V_1 - \left(j\frac{2}{\omega} + \frac{\omega_1(1+\beta_1)}{\omega^2 Q_1}\right)\frac{\mathrm{d}V_1}{\mathrm{d}t} - \frac{k_1}{2}V_2 = 0. \tag{24}$$

Thus, the time-domain equations in Eq. (2) can be simplified as:

$$\begin{cases} \lambda_1 V_1 + \tau_1\dfrac{\mathrm{d}V_1}{\mathrm{d}t} - \dfrac{k_1}{2}V_2 = I_1 \\ -\dfrac{k_{i-1}}{2}V_{i-1} + \lambda_i V_i + \tau_i\dfrac{\mathrm{d}V_i}{\mathrm{d}t} - \dfrac{k_i}{2}V_{i+1} = I_i, \\ -\dfrac{k_{n-1}}{2}V_{n-1} + \lambda_n V_n + \tau_n\dfrac{\mathrm{d}V_n}{\mathrm{d}t} = I_n \end{cases} \tag{25}$$

where

$$\tau_i = -j\frac{2}{\omega} - \frac{\omega_i(1+\beta_i)}{\omega^2 Q_i}. \tag{26}$$

Equation (25) can be solved numerically using the first-order Euler or fourth-order Runge–Kutta methods. Therefore, the field distribution with beam loading in the unsteady state can be calculated, and the beam parameters can be further solved using the beam dynamic equations in Appendix D. Equation (25) is derived from the magnetic coupling model, and the equations for the electric coupling model can be derived in the same manner, which is not shown.

This method is used to calculate the pulse current from the measured input pulses. We are also developing this method to calculate beam parameters such as the energy spread and charge of the macro pulse in a short-pulse operation scenario.

Appendix D: Beam dynamics calculation in accelerating structures

On the axis of an accelerating structure, only the longitudinal electric field accelerates the electron, therefore:

$$\frac{\mathrm{d}(\gamma m_\mathrm{e}c^2)}{\mathrm{d}z} = \Re\left\{eE_z(z)e^{j\phi(z)}\right\} \tag{27}$$

where γ is the relativistic factor, m_e is the rest mass of the electron, c is the speed of light, E_z is the complex amplitude of the longitudinal electric field at $t = 0$, and ϕ is the phase variation when the electron arrives at z from its origin. Applying the differential to ϕ:

$$\frac{\mathrm{d}\phi}{\mathrm{d}z} = \omega\frac{\mathrm{d}t(z)}{\mathrm{d}z} = \frac{\omega}{c}\frac{1}{\beta}. \tag{28}$$

Here, β is the relative speed of the electron. Therefore, the longitudinal beam dynamic equation is:

$$\begin{cases} \gamma' = \Re\left\{E_z^*(z)e^{j\phi(z)}\right\} \\ \phi' = \frac{2\pi}{\lambda}\frac{\gamma}{\sqrt{\gamma^2-1}} \end{cases} \tag{29}$$

where $E_z^* = eE_z/(m_\mathrm{e}c^2)$.

The transverse dynamic equation for a single electron in the accelerating structure is:

$$\frac{\mathrm{d}p_\mathrm{r}}{\mathrm{d}z} = \Re\left\{\frac{eE_\mathrm{r}}{\beta_e c}e^{j\phi} - eB_\theta e^{j\phi}\right\}. \tag{30}$$

Applying linear approximation, the transverse field can be expressed using the longitudinal field [38]:

$$E_\mathrm{r} = -\frac{1}{2}\frac{\partial E_z}{\partial z}r. \tag{31}$$

$$B_\theta = \frac{1}{2c^2}\frac{\partial E_z}{\partial t}r = \frac{j\omega}{2c^2}E_z r. \tag{32}$$

Equation (30) can be written as

$$\frac{\mathrm{d}p_\mathrm{r}^*}{\mathrm{d}z} + N(z)r = 0. \tag{33}$$

where $p_\mathrm{r}^* = p_\mathrm{r}/(m_\mathrm{e}c)$, and

$$N(z) = \frac{1}{2\beta}\Re\left\{\frac{\partial E_z^*}{\partial z}e^{j\phi}\right\} + \frac{\omega}{2c}\Re\left\{jE_z^*e^{j\phi}\right\} \tag{34}$$

When considering the space-charge effect, $N(z)$ has an additional term. In this study, we use the infinite cylinder model [38], and the additional term is

$$\frac{ei}{2\pi R_\mathrm{s}^2\gamma^2\beta c\varepsilon_0}, \tag{35}$$

where i is the beam current, R_s is the beam radius, and ε_0 is the vacuum permittivity.

The maximum radius of the electron bunch in a buncher is of great significance. By analyzing the phase-space ellipse, the equation of the maximum radius R is [38]:

$$\frac{\mathrm{d}^2R}{\mathrm{d}z^2} + \frac{(\beta\gamma)'}{\beta\gamma}\frac{\mathrm{d}R}{\mathrm{d}z} + \frac{N(z)}{\beta\gamma}R - \frac{\varepsilon^2}{R^3(\beta\gamma)^2} = 0. \tag{36}$$

Here, ε denotes the normalized emittance of the beam. The transverse envelope of the beam can be obtained by solving the above equation. Although many codes can deal with beam dynamic calculation [39–41], this method was selected in this study because it is easier to integrate with the equivalent circuit model.

Author contributions All authors contributed to the study's conception and design. Xian-Cai Lin, Qiang Gao, Fang-Jun Hu, and Qing-Zhu Li performed the material preparation, data collection, and analysis. Xian-Cai Lin wrote the first draft of the manuscript, and all authors commented on previous manuscript versions. All authors have read and approved the final manuscript.

Data availability The data that support the findings of this study are openly available in Science Data Bank at https://cstr.cn/31253.11.sciencedb.j00186.00397 and https://doi.org/https://doi.org/10.57760/sciencedb.j00186.00397.

Declarations

Conflict of interest Jia-Ru Shi is an editorial board member for Nuclear Science and Techniques and was not involved in the editorial review or the decision to publish this article. All authors declare that there are no competing interests.

References

1. R. Atun, D.A. Jaffray, M.B. Barton et al., Expanding global access to radiotherapy. Lancet Oncol. **16**, 1153–1186 (2015). https://doi.org/10.1016/S1470-2045(15)00222-3
2. H. Sung, J. Ferlay, R.L. Siegel et al., Global cancer statistics 2020: GLOBOCAN estimates of incidence and mortality worldwide for 36 cancers in 185 countries. CA Cancer J. Clin. **71**, 209–249 (2021). https://doi.org/10.3322/caac.21660
3. V. Favaudon, L. Caplier, V. Monceau et al., Ultrahigh dose-rate FLASH irradiation increases the differential response between normal and tumor tissue in mice. Sci. Transl. Med. **6**, 245 (2014). https://doi.org/10.1126/scitranslmed.3008973
4. B. Lin, F. Gao, Y. Yang et al., FLASH radiotherapy: history and future. Front. Oncol. **11**, 644400 (2021). https://doi.org/10.3389/fonc.2021.644400
5. F. Gao, Y. Yang, H. Zhu et al., First demonstration of the FLASH effect with ultrahigh dose rate high-energy X-rays. Radiother. Oncol. **166**, 44–50 (2022). https://doi.org/10.1016/j.radonc.2021.11.004
6. F.C. Liu, J.R. Shi, H. Zha et al., Development of a compact linear accelerator to generate ultrahigh dose rate high-energy X-rays for FLASH radiotherapy applications. Med. Phys. **50**, 1680 (2023). https://doi.org/10.1002/mp.16199
7. J. Bourhis, W.J. Sozzi, P.G. Jorge et al., Treatment of a first patient with FLASH-radiotherapy. Radiother. Oncol. **139**, 18–22 (2019). https://doi.org/10.1016/j.radonc.2019.06.019
8. P.G. Maxim, S.G. Tantawi, B.W. Loo Jr., PHASER: a platform for clinical translation of FLASH cancer radiotherapy. Radiother. Oncol. **139**, 28–33 (2019). https://doi.org/10.1016/j.radonc.2019.05.005
9. W.-C. Fang, X.-X. Huang, J.-H. Tan et al., Proton linac-based therapy facility for ultra-high dose rate (FLASH) treatment. Nucl. Sci. Tech. **32**, 34 (2021). https://doi.org/10.1007/s41365-021-00872-4
10. A.E. Mascia, E.C. Daugherty, Y. Zhang et al., Proton FLASH radiotherapy for the treatment of symptomatic bone metastases: The FAST-01 nonrandomized trial. JAMA Oncol. **9**, 62–69 (2023). https://doi.org/10.1001/jamaoncol.2022.5843
11. C. Desrosiers, V. Moskvin, A.F. Bielajew et al., 150–250 MeV electron beams in radiation therapy. Phys. Med. Biol. **45**, 1781–1805 (2000). https://doi.org/10.1088/0031-9155/45/7/306
12. L. Papiez, C. DesRosiers, V. Moskvin, Very high energy electrons (50–250 MeV) and radiation therapy. Technol. Cancer Res. Treat. **1**, 105 (2002). https://doi.org/10.1177/153303460200100202
13. C. Yeboah, G.A. Sandison, Optimized treatment planning for prostate cancer comparing IMPT, VHEET and 15 MV IMXT. Phys. Med. Biol. **47**, 2247–2261 (2002). https://doi.org/10.1088/0031-9155/47/13/305
14. A. Sarti, P. De Maria, G. Battistoni et al., Deep seated tumour treatments with electrons of high energy delivered at FLASH rates: the example of prostate cancer. Front. Oncol. **11**, 777852 (2021). https://doi.org/10.3389/fonc.2021.777852
15. A. Lagzda, D. Angal-Kalinin, J. Jones et al., Influence of heterogeneous media on very high energy electron (VHEE) dose penetration and a Monte Carlo-based comparison with existing radiotherapy modalities. Nucl. Instrum. Methods Phys. Res. Sect. B **482**, 70–81 (2020). https://doi.org/10.1016/j.nimb.2020.09.008
16. R.M. Jones, K. Small, D. Angal-Kalinin et al., Evaluating very high energy electron RBE from nanodosimetric pBR322 plasmid DNA damage. Sci. Rep. **11**, 3341 (2021). https://doi.org/10.1038/s41598-021-82772-6
17. https://cerncourier.com/a/adapting-clic-tech-for-flash-therapy/
18. X.-C. Lin, H. Zha, J.-R. Shi et al., Fabrication, tuning, and high-gradient testing of an X-band traveling-wave accelerating structure for VIGAS. Nucl. Sci. Tech. **33**, 102 (2022). https://doi.org/10.1007/s41365-022-01086-y
19. X. Lin, H. Zha, J. Shi et al., X-band two-stage rf pulse compression system with correction cavity chain. Phys. Rev. Accel. Beams **25**, 120401 (2022). https://doi.org/10.1103/PhysRevAccelBeams.25.120401
20. P. Girault, The 3 pi /4 backward TW structure for the ELETTRA 1.5 GeV electron injector. in *Conference Record of the 1991 IEEE Particle Accelerator Conference* (1991). https://doi.org/10.1109/PAC.1991.165267
21. S. Zheng, *Dissertation* (Tsinghua University, 2000)
22. A. Vnuchenko, D. Esperante Pereira, B. Gimeno Martinez et al., High-gradient testing of an S-band, normal-conducting low phase velocity accelerating structure. Phys. Rev. Accel. Beams **23**, 084801 (2020). https://doi.org/10.1103/PhysRevAccelBeams.23.084801
23. A. Araujo Martinez, R. Agustsson, S. Kutsaev et al., High-gradient accelerating structure for hadron therapy Linac, operating at kHz repetition rates, in *LINAC2022* (2022) https://doi.org/10.18429/JACoW-LINAC2022-MOPOPA22
24. J. Liu, J. Shi, A. Grudiev et al., Analytic RF design of a linear accelerator with a SLED-I type RF pulse compressor. Nucl. Sci. Tech. **31**, 107 (2020). https://doi.org/10.1007/s41365-020-00815-5
25. J. Shi, S. Zheng, H. Chen, Calculating field distribution of a linear accelerator using equivalent circuit model. High Energy Phys. Nuclear Phys. (2006). https://doi.org/10.3321/j.issn:0254-3052.2006.07.024
26. https://www.cst.com
27. C.W. Steele, A nonresonant perturbation theory. IEEE Trans. Microwave Theory Tech. **14**, 70–74 (1966). https://doi.org/10.1109/TMTT.1966.1126168
28. C.K. Gong, S.X. Zheng, J.H. Shao et al., A tuning method for nonuniform traveling-wave accelerating structures. Chin. Phys. C **37**, 9–12 (2013). https://doi.org/10.1088/1674-1137/37/1/017003
29. M. Peng, J. Shi, H. Zha et al., Development and high-gradient test of a two-half accelerator structure. Nucl. Sci. Tech. **32**, 60 (2021). https://doi.org/10.1007/s41365-021-00895-x
30. D. Nagle, *Coupled resonator model of linear accelerator tanks* (Los Alamos Scientific Lab, 1964)
31. E.A. Knapp, Design, construction, and testing of RF structures for a proton linear accelerator. IEEE Trans. Nucl. Sci. **12**, 118–127 (1965). https://doi.org/10.1109/tns.1965.4323604
32. D. Nagle, E. Knapp, B.J.R.O.S.I. Knapp, Coupled resonator model for standing wave accelerator tanks. Rev. Sci. Instrum. **38**, 1583–1587 (1967). https://doi.org/10.1063/1.1720608
33. W.E. Jule, R.L. Gluckstern, Equivalent circuit for a perturbed multi-cell structure. IEEE Trans. Nucl. Sci. **20**, 943–948 (1973). https://doi.org/10.1109/TNS.1973.4327295
34. J. Sekutowicz, S. Kuliński, M. Pachan, Frequency dependent capacitive-inductive model for axially coupled $\pi/2$ standing wave biperiodic structures. IEEE Trans. Nucl. Sci. **32**, 2824–2827 (1985). https://doi.org/10.1109/tns.1985.4334194
35. L.-Y. Zhou, H. Zha, J.-R. Shi et al., A non-invasive diagnostic method of cavity detuning based on a convolutional neural network. Nucl. Sci. Tech. **33**, 94 (2022). https://doi.org/10.1007/s41365-022-01069-z
36. J. Shi, S. Zheng, H. Chen et al., Calculating RF parameters of individual cell by electric field distribution of a coupled cavity chain. High Energy Phys. Nuclear Phys. **29**, 818–823 (2005). https://doi.org/10.3321/j.issn:0254-3052.2005.08.020
37. X.-C. Lin, H. Zha, J.-R. Shi et al., Design, fabrication, and testing of low-group-velocity S-band traveling-wave accelerating structure. Nucl. Sci. Tech. **33**, 147 (2022). https://doi.org/10.1007/s41365-022-01124-9
38. N. Liu, *Accelerator theory* (Tsinghua University Press, 2004)

39. L. Young and J. Billen, The particle tracking code Parmela. in *Proceedings of the 2003 Particle Accelerator Conference* (2003) https://doi.org/10.1109/PAC.2003.1289968
40. S.V. Kutsaev, Electron dynamics simulations with Hellweg 2D code. Nucl. Instrum. Methods Phys. Res. Sect. A **618**, 298–305 (2010). https://doi.org/10.1016/j.nima.2010.02.090
41. K. Flottmann, ASTRA: A space charge tracking algorithm (2011)